CRYPTS-ON-A-CHIP:
DEVELOPING AN *EX VIVO* MODEL OF THE INTESTINAL CRYPTS

Brent Jacob Puthoff

A thesis submitted to the faculty of the University of North Carolina at Chapel Hill and North Carolina State University in partial fulfillment of the requirements for the degree of Masters of Science in the Department of Biomedical Engineering.

Chapel Hill
2012

Approved By:

Scott T. Magness, Ph.D.

Nancy Allbritton, MD. Ph.D.

Glenn Walker, Ph.D.

ABSTRACT

BRENT JACOB PUTHOFF: Crypts-on-a-Chip: Developing an *ex vivo* Model of the Intestinal Crypts

Currently, stem cell behavior following injury, inflammation, and viral/bacterial challenge is difficult to study *in vivo* due to the inability to control variables, limited human tissue resources, the prohibitive costs involved with animal studies, and/or the lack of cross-species infection by species-specific microbes. The goal of this thesis is to develop an *ex vivo* model of the gut epithelium and underlying mesenchyme to facilitate studies that are not possible due to these technical, ethical, and financial constraints. Microfabricated well arrays that mimic intestinal crypt dimensions demonstrated that PDLA, polystyrene, and 1002F promote proliferation of gut myofibroblasts more rapidly than PDMS. Methods were developed to enhance crypt seeding into microwells and standardize the isolation of epithelial tissue. Advanced 3-D imaging techniques using multi-photon excitation (MPE) and Imaris were also developed. These studies are a stepping stone in the development of an organ-on-a-chip for the intestine, and provide proof of concept for intestinal tissue engineering with microfabricated scaffolds.

ACKNOWLEDGEMENTS

Dr. Scott Magness for guidance, mentorship, and constructively challenging me.

Dr. Susan Henning, Dr. Nancy Allbritton, Dr. Glenn Walker, Dr. Yuli Wang and Dr. Sharon Lubkin: who's wealth of knowledge provided very helpful advice, direction, and support of this work.

Dr. Yuli Wang and Joe Balowski for most of the design and fabrication of the scaffolds used in this work.

Megan Fuller, Richard von Furstenberg, Adam Gracz, Dr. Victoria Bali, Ian Williamson, and everyone in the UNC GI Stem Cell Group for their support of this work and thoughtful advice and suggestions.

My family and friends for their constant support and encouragement, especially my sister Andrea Borchers, and my brother-in-law Scott Borchers.

TABLE OF CONTENTS

LIST OF TABLES

LIST OF FIGURES

LIST OF SYMBOLS AND ABBREVIATIONS

Unit Prefixes

Symbol	*Value*
n	$x10^{-9}$
µ	$x10^{-6}$
m	$x10^{-3}$
c	$x10^{-2}$
k	$x10^{3}$

Units

Symbol	*Name*
g	gram
s	second
m	meter
M	mole
^{o}C	degrees Celsius
G	gravity

Abbreviations

APC	allophycocyanin
Ascl2	achaete-scute complex homolog 2
BAC	bacterial artificial chromosome
BFP	blue fluorescent protein
CBC	crypt base columnar
CD	cluster of differentiation
CFP	cyan fluorescent protein
DMEM	Dulbecco's modified eagle medium
DPBS	Dulbecco's phosphate buffered solution
DTT	Dithiothreitol
ECM	extra cellular matrix
EDTA	ethylenediaminetetraacetic acid

Abbreviations continued

EE	enteroendocrine
EGFP	enhanced green fluorescent protein
EpCAM	epithelial cell adhesion molecule
FACS	fluorescence-activated cell sorting
FBS	fetal bovine serum
FDA	US Food and Drug Administration
GENSAT	gene expression nervous system atlas
GI	gastrointestinal
HBSS	Hank's buffered saline solution
IESC	intestinal epithelial stem cell
Lgr5	leucine-rich repeat containing G-protein coupled receptor 5
LSM	laser scanning microscope
MEF	murine embryonic fibroblast
MF	myofibroblast
MPE	multi-photon excitation
OCT	optimal cutting temperature
Olfm4	Olfactomedin 4
PDLA	Poly (DL-lactide)
PDMS	polydimethylsiloxane
PFA	paraformaldehyde
PI	Propidium iodide
RFP	red fluorescent protein
SDC	spinning-disk confocal
SMA	smooth muscle actin
Sox	*Sry*-Box-containing
Sry	Sex determining region Y
TA	Transit-amplifying
UV	ultraviolet
YFP	yellow fluorescent protein

CHAPTER 1

INTRODUCTION

In recent years, there has been significant interest in the development of *ex vivo* living models of organ systems of the human body [1, 2]. Animal models, especially rodent, have been a standard for biomedical research, however technical, ethical, and financial constraints limit the types of research that can be performed. An *ex vivo* organ model would not completely replace animal models, but could be used as a supplement for researchers to gain a better understanding of organ development and response to stimuli. Previous work has shown the ability to create organ-on-a-chip models using cells from the lung, liver, and gastrointestinal (GI) tract [3-5]. Many of these models, especially those of the GI tract, do not recreate the microanatomy of the organ as they are essentially a monolayer of cells plated on a chip. The goal of this work was to develop an *ex vivo* model that recapitulated the anatomy and physiology of the crypts and underlying mesenchyme of the intestine.

With the recent interest and potential benefits of organ-on-a-chip models, the National Institute of Health and the Defense Advanced Research Projects Agency (DARPA) have made the development of these models a priority by allocating more than $100 million dollars towards their development. These agencies have set forth guidelines for organ-on-a-chip models developed with these research dollars. The models should be modular, that is, important components should be interchangeable to allow easy integration with other organ-on-a-chip systems. Techniques to create the models should be easily reproducible. The models should remain viable for four weeks to allow scientifically relevant analysis. Finally,

the organ-on-a-chip models should allow seamless integration with various imaging modalities.

Organ-on-a-chip models offer researchers several benefits over animal models. First, the models give researchers the ability to tightly control variables. In a mouse model, cellular signaling, gut microbiota, the immune response, and other factors can influence experimental results. By tightly controlling these variables, researchers can pinpoint the molecule or signaling pathway that caused an experimental outcome, which is particulary useful if that outcome is promising. Tight variable control is especially powerful for studying stem cell genetics, as Wnt signaling or the gradients of mitogens and morphogens can be very carefully controlled, allowing the analysis of the proliferation and differentiation of the stem cell population.

Ethical sentiments and FDA guidelines also prevent most research on human patients. However, small tissue samples could be extracted, expanded *in vitro*, and seeded onto a supporting layer to create an *ex vivo* system. Rather than interpreting and extrapolating the results from an animal model experiment, an *ex vivo* model composed of human tissue would allow researchers to more accurately study the response of the human tissue to pharmaceuticals, carcinogens, or pathogenic microbes.

With the current emphasis on individualized medicine, an *ex vivo* could be an additional safeguard employed prior to the administration of a new treatment to a patient. Biopsies of diseased tissue could be excised from a patient and cultured as multiple *ex vivo* models. Each model could then be subjected to a unique pharmaceutical combination, and the results used to help identify an effective treatment regimen for the patient.

The primary barriers of pharmaceutical development and approval could be lowered as these models would reduce the time and cost associated with the current large format screening process of novel nanoparticles or pharmaceuticals. The *ex vivo* system can be compartmentalized allowing the study of a dozen or more pharmaceuticals simultaneously. Labor and material costs can be reduced by minimizing the time, space, and expensive reagents required for these screening procedures. Screening with an ex vivo human tissue model also gives researchers the ability to test pharmaceuticals earlier in the three phase clinical trial schedule. The majority of the drugs shown to be safe in animal models fail in phase III clinical trials, therefore, testing the pharmaceuticals on a human *ex vivo* model could eliminate some of the unsuccessful drugs earlier and save overall drug development outlays [4].

Successful development of an *ex vivo* model of the intestinal crypts requires a deep understanding of the anatomy and physiology of the intestine, which is a very complex organ consisting of layers of muscle, submucosa, and epithelial layer, with an intricate system of nerves and blood vessels. The intestinal crypts are invaginations in the intestinal epithelium and are the proliferative portion of the epithelial layer (Figure 1). The other portion of the

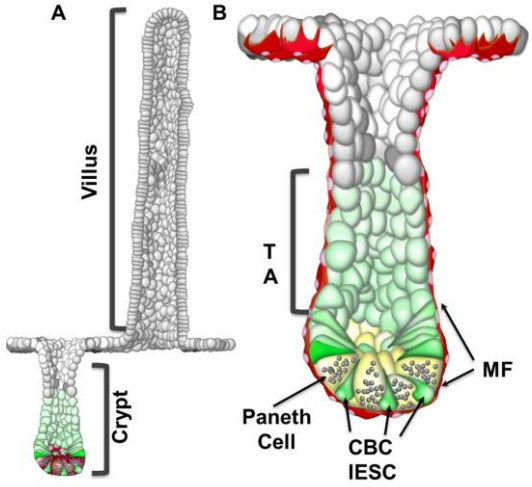

Figure 1 – Microanatomy of the small intestine epithelium and stem cell niche. (A) View of a crypt villus unit. Cells are born in the crypt, migrate to the villus tip, and slough into the intestinal lumen. (B) Schematic of the crypt identifying the location of key cell types: the CBC IESCs, Transit-amplifying progenitors (TA), myofibroblasts (MF), and the Paneth cells.

intestinal epithelial layer, villi, are finger-like protrusions which extend into the lumen and absorb nutrients from food ingested by the organism.

The intestinal epithelium is maintained by a pool of stem cells at the base of the crypt called crypt base columnar cells (CBCs), also referred to as intestinal epithelial stem cells (IESCs). The CBCs typically divide asymmetrically to generate more rapidly dividing transit-amplyfying (TA) progenitor cells located above the IESCs in the crypt. These progenitor cells commit to one of four distinct cell types: the enterocyte (absorptive), goblet cell (mucous-producing), enteroendocrine (EE, hormone-producing), and Paneth cell (antimicrobial-peptide-producing). Paneth cells migrate toward the base of the crypt, while the other cells types migrate up the length of the villi, where they are sloughed off into the lumen. This cell division, differentiation, and transit process is very rapid, and regenerates the entire intestinal epithelium every 3-7 days. Underlying the epithelium is a layer of myofibroblasts, which support the epithelium through extra cellular matrix (ECM) production and extrinsic signaling [6, 7].

In previous studies, we have shown the ability to isolate IESCs using a Sox9 extra green fluorescent protein (EGFP) reporter mouse model developed in our lab in which the stem cells have a fluorescence level characterized as Sox9EGFP^{low}. After isolation, the IESCs have been successfully cultured *in vitro* into crypt/villus-like units termed 'enteroids,' which consist of all four cell types of the intestinal epithelium. There are a few limitations, though, of the *in vitro* model. The success rate, as defined by enteroid formation divided by plated cells, has been quite low. The enteroids also form into irregular enclosed shapes that hinder their study (Figure 2).

This low culture efficiency and the uneven and inconsistent shape of the enteroids creates the necessity to develop tools that would allow for a more representative and functional *ex vivo* model of the epithelium. A supporting layer, called a scaffold, can be employed for more systematic placement of the epithelial tissue. Previous studies have shown that multiple layers can be cultured on these scaffolds allowing the directed differentiation and expansion of stem cells [8]. Microfabrication techniques were used in the production of the scaffolds as they are capable of high spatial resolution which allows the recreation of the intricate architecture of the endogenous intestinal epithelium [9].

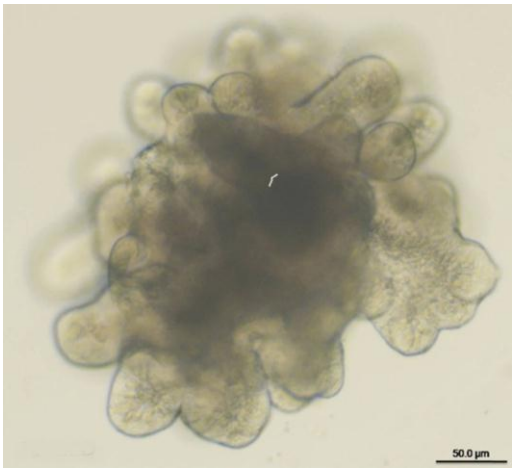

Figure 2. Enteroid cultured in 3-D protein matrix. Crypt buds are around the outer surface of the enteroids and the dark area in the center is the pseudolumen where apoptotic cells are sloughed off.

Thesis Overview

The following chapters detail the methodology and experiments that were performed in the development of an *ex vivo* model of the intestinal crypts. Chapter 2 details the considerations and experiments involved in selecting a scaffold material and determining the geometry of the scaffold that promotes monolayer formation. Chapter 3 presents our work to characterize and optimize the isolation and culture of epithelial cells from murine mouse models. This work is necessary for the reproducibility of the *ex vivo* model, allowing quantitative scientific study and analysis. Chapter 4 describes our work to develop novel imaging and modeling of the *ex vivo* system. Chapter 5 includes conclusions and suggestions for future work.

CHAPTER 2

SCAFFOLD DEVELOPMENT

INTRODUCTION

The establishment of a favorable environment and niche for the IESCs is essential to generating *ex vivo* intestinal epithelial tissue. This niche is thought to consist of the IESCs themselves, paneth cells also located at the base of the crypt, and the underlying myofibroblasts. Extrinsic signaling between these cell types is generally considered necessary for the proper expansion of the intestinal epithelial layer [6, 7, 10]. Recreating this stem cell niche *ex vivo* requires determining the properties that are essential to generating a consistent and persistent monolayer of myofibroblasts on the scaffold.

An important consideration in generating this niche is determining a scaffold material that will allow proper adhesion and proliferation of the myofibroblasts and epithelial cells. To generate the complex architecture of the intestine, microfabrication was chosen for its high spatial resolution capabilities, allowing replication of the physical structure of the *in vivo* environment [11]. Microfabrication is a technique that was developed out of the microprocessor industry and allows the formation of 3-D structures at the micron scale and can be fabricated with techniques including soft lithography, photolithography, and chemical etching.

Four scaffold materials were considered based on their compatibility with microfabrication: a) polydimethlysiloxane (PDMS); b) polystyrene; c) Poly (DL-lactide) (PDLA); and d) 1002F. PDMS is often used for microfabrication due to its ease of manipulation and optical clarity [12]. Polystyrene is frequently used in tissue culture because of its low cost, optical clarity, chemical inertness, and cell adhesion properties when chemically functionalized [13, 14]. Techniques have recently been developed to allow polystyrene fabrication via soft lithography, making it more attractive for microfabrication prototyping and research [15]. PDLA has been FDA approved for implantation, therefore, it is often selected as a scaffold material for tissue engineering applications. The fourth material studied, 1002F, is a photoreactive material and, thus, photolithography can be employed for its fabrication. Photolithography allows the fabrication of features as small as 10 μm in diameter, which some of the designs presented in this work required. 1002F is also less auto-fluorescent than the more commonly used SU-8 [13], making it more desirable for our application since imaging compatibility is a key requirement of the *ex vivo* model.

After successful development of the scaffold architecture, the mesenchymal layer, that is, the myofibroblast monolayer, needed to be established. An extra cellular matrix (ECM) component, bovine gelatin, was seeded onto the scaffold to facilitate adhesion of the myofibroblasts. The age of the pups used for myofibroblast harvest was also considered. Murine embryonic fibroblasts (MEF) are often used as feeder cells for stem cell culture *in vitro* as they provide the correct signaling for single stem cells. This research, however, focused on the seeding of intact crypts, not single stem cells. For the intact crypts, the goal of the culture is more focused on retaining viability of the epithelial cells rather than proper proliferation and differentiation of the stem cells. To facilitate this crypt homeostasis,

myofibroblasts from 4 to 6-day old pups were utilized as they are more developmentally mature. Myofibroblasts from this age pups have successfully been used in previous small intestine tissue engineering applications [16] and they also eliminate the need to sacrifice the mother, which can reduce mouse costs.

Another critical parameter in developing the scaffold is the size of wells for the *ex vivo* crypts. Isolated murine crypts average 45 μm in cross-sectional diameter and 190 μm in length (data not shown). Ideally, an intestinal scaffold would contain synthetic microwells of the same size; previous studies have noted, however, that fibroblasts obstructed the openings when cultured in wells less than 200 μm in diameter [8]. The diameter of the wells were varied to determine a size that would: a) allow a consistent monolayer to form; b) allow the diffusion of key nutrients to the tissue within the wells; and c) allow epithelial tissue to seed into the biological scaffold.

The surface of the microfabricated scaffolds is substantially increased by the array of synthetic crypt microwells. Both Table 1 and Figure 3 depict the increase in surface area of the scaffolds over a flat surface when varying the depth and diameter of the microwells. This increase in surface area is of utmost importance when considering the number of seeded myofibroblasts required to generate a consistent monolayer.

Table 1. Scaffold surface area increase for varying diameters and depths of microwells.

Diameter of Microwell (μm)=	100			150			200		
Depth of Microwell (μm)=	100	150	200	100	150	200	100	150	200
Spacing (OD to OD) (μm)=	25	25	25	25	25	25	25	25	25
Surface area of one microwell (sq. μm)=	39,270	54,978	70,686	64,795	88,357	111,919	94,248	125,664	157,080
Surface area of flat surface (sq. μm)=	15,625	15,625	15,625	30,625	30,625	30,625	50,625	50,625	50,625
Surface area of microwell surface (sq. μm)=	47,041	62,749	78,457	77,749	101,311	124,873	113,457	144,873	176,289
Microwell surface area relative to flat surface (%) =	301	402	502	254	331	408	224	286	348

The diffusion of key nutrients into the sub-mm size of the microwells was also a concern. Intestinal fibroblasts require nutrients, especially glucose and glutamine, to maintain cellular homeostasis [17]. Comsol, a differential equation modeling software, was used to verify that both glucose and glutamine diffused into the microwells at a sufficient rate to promote equilibrium. Due to the large increase in surface area of the scaffolds and the additional number of fibroblasts required to create a monolayer, we also calculated the total amount of nutrients that would be consumed by the myofibroblasts in culture.

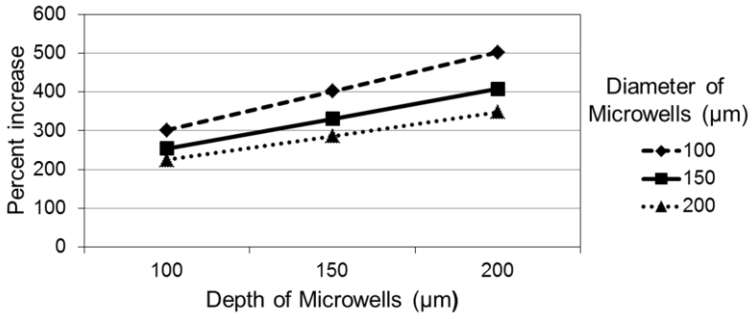

Figure 3. Graphical representation of the scaffold surface area increase.

The microwells also had to be of sufficient diameter to allow epithelial tissue to seed into them following myofibroblast seeding. Single intestinal epithelial stem cells (IESCs) and intact crypts were considered as potential options for seeding onto the biological scaffolds. IESCs are smaller and, thus, have higher seeding rates than intact crypts. However, intact crypts have higher culture efficiencies, shorter and less expensive isolation since cell sorting is not required, and can be used with any mouse model since stem cells do not need to be isolated. With these considerations, the benefits of intact crypts outweighed those for single cells, and this research focused on intact crypts.

MATERIALS AND METHODS

Scaffold Materials

Polystyrene used for microfabrication in these studies was obtained and prepared as previously described [15]. PDLA was purchased from Purac (Lincolnshire, IL) and is sold commercially as Purasorb PDL 05. PDMS was prepared from the Sylgard 184 silicone elastomer kit (Dow Corning, Midland, MI).

Formulation of 1002F photoresist

Microstrainers were manufactured with 1002F photoresist, which was formulated by mixing 1002F resin, photoinitiator (triarylsulfonium hexafluoroantimonate salts), and solvent (γ-butyrolactone) as previously described [13]. The weight ratio of resin : photoinitiator : solvent was 49 : 4.9 : 46.1 for formulation 10, and 64 : 29.6 : 6.4 for formulation 100. Formulation 10 and 100 generated 1002F film thickness of around 10 and 100 μm, respectively, when the spin coating speed was set at 2000 rpm.

Microstrainer Fabrication

Methodology for the fabrication of the microstrainers is described in a previous publication [18]. Figure 4 shows a detailed schematic of the fabrication process to create the microstrainers, which was a two-layer process. A 1002F film of 10-μm thickness was spin-coated on a clean glass slide at 2000 rpm using 1002F photoresist (formulation 10) (Figure 4-ii). After baking at 95 °C for 10 min, the film was exposed to UV light at a dose of 1000 mJ/cm^2 (Figure 4-iii). The post-exposure baking was performed in a 95 °C oven for 5 min

followed by a 120 °C hotplate for 5 min. The sample was then developed for 45 sec, and baked on a 120 °C hotplate for 60 min (Figure 4-iv). To prevent trapping of air bubbles during the second layer coating step, the sample was treated with air plasma for 5 min to make its surface hydrophilic. A second 1002F layer of 100-µm thickness was spin-coated at 2000 rpm using 1002F photoresist formulation 100 (Figure 4-v), baked at 95 °C for 60 min, exposed to UV light at a dose of 1000 mJ/cm^2 (Figure 4-vi), post-exposure baked at 95 °C for 10 min, and then developed for 15 min (Figure 4-vii). The film was solidified by baking it on a 120 °C hotplate for 60 min. Finally, the sample was soaked in a soap solution overnight to facilitate release of the freestanding film from the glass slide (Figure 4-viii). The solid bottom wells were fabricated with the same process, except that the entire 10 µm thick bottom layer was exposed to UV light to create a surface without any openings.

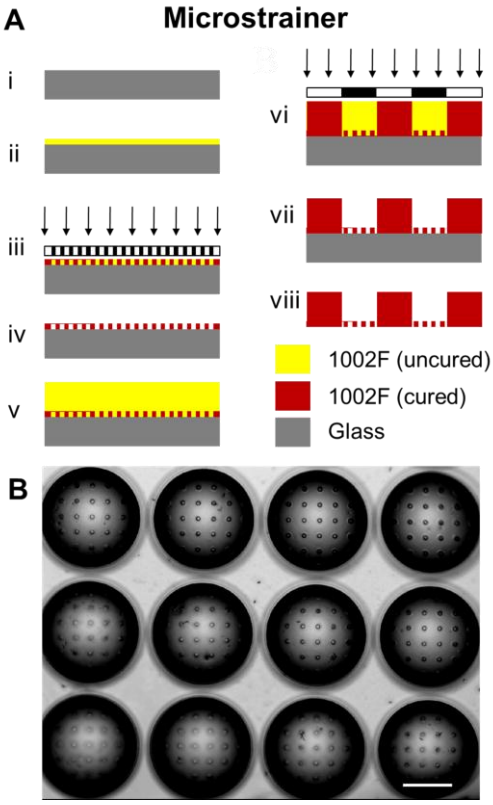

Figure 4. Microstrainer array. A: Schematic of the microstrainer array fabrication process. B: Brightfield image of the completed microstrainers. Scale bar is 100 um.

Mice/Genotyping

All mice used in this study were maintained on a 12:12-h light-dark cycle in American Association for Accreditation of Laboratory Animal Care-approved facilities. CD-1 mice were used for myofibroblast isolation. Sox9EGFP mice were used for intestinal crypt isolation. The Sox9EGFP mouse line contains genomic integration of a modified BAC

(RP32-140-D18) with ~75.5kb upstream and ~151kb downstream sequence to Sox9. This mouse line was initially created as part of the GENSAT Brain Atlas Project [19]. Frozen Sox9EGFP mouse embryos were obtained from the Mutant Mouse Regional Resource Center at the University of California at Davis and were reconstituted by transfer into foster mice. This mouse strain was maintained as heterozygotes on the CD-1 genetic background. Mice bred normally and progressed to adulthood without any overt phenotypes due to the transgene. About 10 days after birth, tails were snipped and viewed under an epi-fluorescent microscope fitted with filters for visualizing EGFP to determine phenotype.

Intestinal crypt isolation

Ten cm of jejunal tissue from 6 to 10 week old Sox9EGFP mice was incubated in PBS containing 4 mM ethylenediaminetetraacetic acid EDTA and 1 mM Dithiothreitol (DTT) for 30 min at 4°C on a rotating platform. Villi were removed by light shaking at a force of 1 to 2 times gravity for 10 back and forth cycles. The tissue was transferred into a tube with PBS. Crypts were released by vigorous shaking (3 to 4 times gravity) at 2.5 to 3 back and forth shake cycles per second for two minutes. Crypts were then passed through a 70 μm filter (Becton Dickenson) to remove larger contaminating villi. Sucrose was added to a final concentration of 4% w/v and the solution was pelleted at 13g for 7 min to remove debris and single cells.

Myofibroblast isolation and culture

Gut myofibroblasts were harvested from 4 to 6-day-old murine CD-1 pups. The small intestine was cut into 2 mm x 2 mm sections and rinsed of debris and fecal matter at 4^{o} C in an orbital shaker for two minutes in DMEM with antibiotics (50 μg/mL Penicillin, 50

mg/mL Streptomycin, P/S). The intestinal fragments were allowed to settle and the supernatant was removed. The wash procedure was repeated 8 times. The intestinal fragments were then minced to 1 mm X 1 mm segments with a new razor blade and added to 6 mL of DMEM with 0.3U/mL dispase (BD Biosciences, Franklin Lakes, NJ), 300 U/ml collagenase I (Sigma), and P/S (50 μg/mL, 50 mg/mL). The resulting solution was placed on an orbital shaker and allowed to incubate at room temperature for 25 min.

After incubation, the myofibroblast isolation procedure consists of a sequential and repetitive dissociation of the same intestinal segments. 10 mL of DMEM with 10% FBS was added to the solution and mixed by pipetting 50 times to break apart the intestinal fragments. The fragments were allowed to settle for 1 min in a 50 mL conical tube and the supernatant was removed and transferred to a new tube. Fresh 10 mL of DMEM with 10% FBS was added to the initial tube with intestinal fragments and the solution was again mixed 50 times by pipetting. After allowing the fragments to settle, the supernatant was removed and combined with the first supernatant. The initial fragments were re-suspended in DMEM and 10% FBS and both solutions were pelleted at 200g. Supernatants were removed and each pellet was re-suspended in 10mL of DMEM with 10% FBS, P/S (50 μg/mL, 50 mg/mL), Gentamicin (50 μg/mL, Sigma), and Glutamax (1X, Gibco). Both cell solutions were plated in a 10 cm plate and the media changed for each of the first two days to minimize the chance of contamination.

Cells were cultured at 37^{o} C in 5% CO_2. After two weeks in culture, the Gentamicin was removed. Media was changed every 3-4 days until the cultures became confluent. When the cultures achieved confluency, they were detached by trypsin, split into 3 equal portions, and replated. Myofibroblasts were passaged at least three times before use to

eliminate non-fibroblastic cells. Cells were used before passage 15, as a transformation to a more muscle-like phenotype was observed around this time.

Material Comparison

Plasma-treated polystyrene was obtained from BD Falcon (Cat# 353043) and used without further treatment. PDMS, PDLA, and 1002F were thinly coated on glass coverslips, cured on a hot plate, and vacuum-gas plasma oxidized for 5 min. Gut myofibroblasts were pipetted onto fifteen samples of each material at 12,000 cells/cm^2. At each time point after the initial plating (1 hour, 24 hours, 2 days, 4 days, and 8 days), three samples of each material were rinsed with PBS to remove non-adherent cells and fixed with PFA. Nuclei were stained with Bisbenzimide (Sigma), and cells were counted in three separate fields of view with fluorescent imaging. Population doubling times of the cell cultures were calculated using the algorithm provided by http://www.doubling-time.com [20].

Statistics

All data are presented as the mean ± SEM.

RESULTS

Gut myofibroblast proliferation is faster with PS, PDLA, and 1002F, than with PDMS

A critical component of tissue engineering is finding the correct scaffold material for each particular tissue type. In developing the *ex vivo* intestinal model, we hypothesized that scaffold material could impact the development of the tissue. We focused primarily on proliferation rates of gut myofibroblasts on polystyrene, PDLA, 1002F, and PDMS, which are compatible with microfabrication.

To determine the proliferation rates of gut myofibroblasts on the four materials, MFs were seeded at 12,000 cells/sq. cm., cultured for eight days, and cell numbers were counted at time points 1 hour, 24 hours, 2 days, and 4 days after the initial plating. The material surfaces had warped by day 8, which likely skewed the cells counts, therefore, cell counts at day 8 are not reported here.

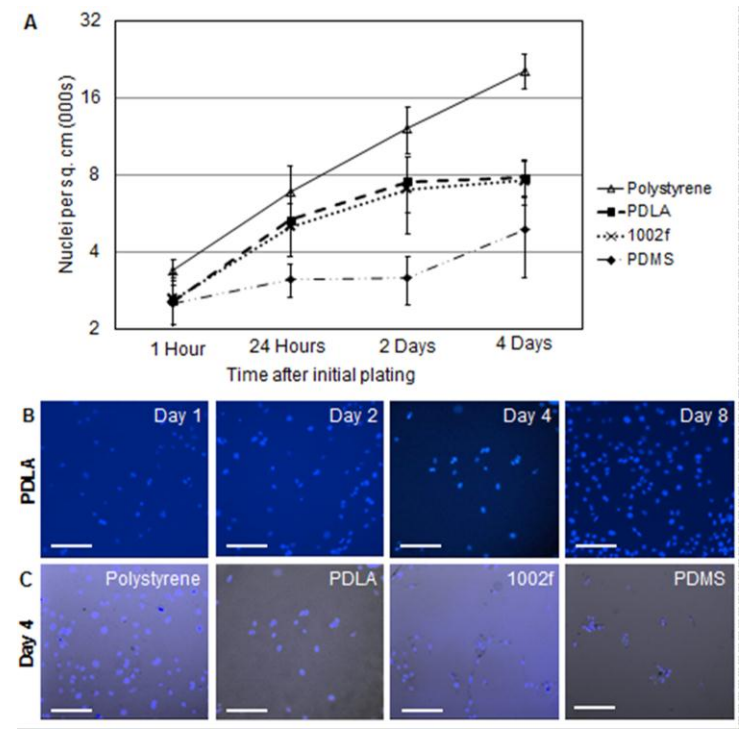

Figure 5. Proliferation of myofibroblasts is more rapid on Polystyrene, PDLA, and 1002F than on PDMS. All scale bars are 200 µm. A: Proliferation of myofibroblasts over time. B: Proliferation and development of the myofibroblast monolayer on PDLA in culture. Nuclei were stained with Bisbenzimide and visualized with DAPI. C: Brightfield and DAPI overlays of the myofibroblasts in culture on Day 4. Myofibroblasts on PDLA, 1002f, and PDMS have formed conglomerates and much of the culture area is not covered by cells. Data are shown as means ± SE (n=3)

Proliferation was the most rapid and logarithmically linear for myofibroblasts cultured on polystyrene. Cell doubling time was 1.82 days for the first four days. The number of myofibroblasts doubled on each of the first two days, followed by a slower proliferation rate, likely due to cell contact inhibition as the MFs approached confluency (Figure 5A) [21]. The fibroblast density also appeared to plateau around 30,000 cells/sq.cm (data not shown). Myofibroblast proliferation rates were slightly slower on both 1002F and PDLA (3.56 and 3.50 days, respectively) and slowest on PDMS (4.29 days). The growth curves were also not as logarithmically linear for MFs cultured on 1002F, PDLA, and PDMS (Figure 5A).

Microwells with 10 µm openings in their base facilitate increased crypt seeding

After verifying that several materials were compatible with gut myofibroblast adhesion and proliferation, the dimensions of the synthetic crypt microwells necessary for myofibroblast monolayer formation and crypt seeding was explored. As stated earlier, murine crypts average 45 µm in diameter, therefore microwells diameters would ideally be near this size to recreate the *in vivo* environment. Preliminary

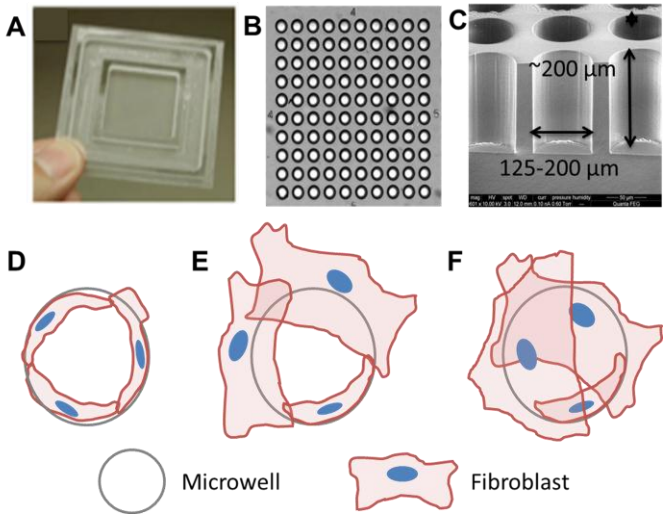

Figure 6. Myofibroblasts seeded onto microfabricated chips with arrays of microwells. A: Microfabricated chips are approximately 2 cm x 2 cm. B: Top view of the microwell arrays. C: Cross-section view of one of the microwells. D: Example of an 'open' microwell. Myofibroblast cell nucleus in blue and cytoplasm in red. E: Partially occluded microwell; open area is greater than the cross-sectional area of a vertical crypt. F: Fully occluded microwell.

experiments showed, however, that myofibroblasts spread over the surface of the chips and occluded microwells with diameters of 50, 75, and 100 µm. To determine a microwell size that would not be occluded by the fibroblasts and would allow crypt seeding, PDLA chips with arrays of microwells were fabricated with diameters ranging from 125 µm to 200 µm (Figure 6 A,B,C). The chips were seeded with myofibroblasts at a density of 60,000 cells/sq. cm and cultured for two days. Light microscopic examination revealed that many of the microwells were either partially or fully occluded by myofibroblasts spanning the opening of the wells (See Figure 6 D,E,F for a graphic representation).

Early experiments showed that very few of the intact crypts successfully seeded into the microwells with solid bottoms after myofibroblasts had been seeded. We hypothesized that openings in the base of the crypt would create a slight flow through the wells and, therefore, increase the number of crypts settling into the wells. Ten-µm diameter circular openings (Figure 7A) were chosen since they are small enough to prevent transit of fibroblasts and crypts, but large enough to allow the passage of fluids. This array of wells with 10-µm openings will be referred to as 'microstrainers', and were fabricated with 1002F as described in the Materials and Methods section.

To determine if microstrainers would increase the number of crypts settling into the wells, fibroblasts were first seeded in both microwells with solid bases and microstrainers at a density of 30,000 cells/cm^2. Intestinal murine crypts were seeded 2 days after the initial fibroblast seeding in a solution of DMEM at 1,000 crypts/mL. (Crypts often aggregated when seeded at densities greater than 1,000 crypts/mL, preventing them from settling into the wells [data not shown]). The crypt solution was pipetted onto the microstrainers and allowed to settle for 15 minutes. This process was repeated until the total number of seeded crypts

equaled half the number of microwells. Seeding more than this set number of crypts would have skewed the seeding efficiency by increasing the chance of multiple crypts settling in one microwell. The probability of any given well containing 0, 1 or 2 crypts is defined by the Poisson distribution:

$$F(k,\lambda) = \frac{\lambda^k e^{-\lambda}}{k!}$$

Where k = number of crypts seeding into a well (in this study, k could be 0,1,2, etc.)

k! = the factorial of k

λ = simple probability that one crypt will seed into a well (i.e., if 10 crypts are seeded into an array of 100 wells, λ would be set at 0.10. λ remains constant for varying values of k. See Table 2 for examples of k and λ values.)

e = base of the natural logarithm (e=2.71828...)

		A= Zero crypts in well			B = Single crypt in well			Two or more crypts in well		
Number of crypts	Number of wells	k	λ	Probability (%)	k	λ	Probability (%)	k	λ	Probability= 100%-A-B
10	100	0	0.06	94.2	1	0.06	5.7	2,3,4…	0.06	0.2
20	100	0	0.12	88.7	1	0.12	10.6	2,3,4…	0.12	0.7
30	100	0	0.18	83.5	1	0.18	15.0	2,3,4…	0.18	1.4
50	**100**	**0**	**0.30**	**74.1**	**1**	**0.30**	**22.2**	**2,3,4…**	**0.30**	**3.7**
75	100	0	0.45	63.8	1	0.45	28.7	2,3,4…	0.45	7.5
100	100	0	0.60	54.9	1	0.60	32.9	2,3,4…	0.60	12.2

Table 2. Crypt seeding probabilities as governed by the Poisson distribution, $F(k,\lambda) = (\lambda^k e^{-\lambda})/k!$. Values are based on a 200 µm diameter well with 25 µm spacing. These dimensions create a surface that is approximately 60% open well and 40% intervening areas. λ was set by assuming that 50% of the surface area of the crypt would need to be positioned above the well to allow the crypt to settle into the well. The percent chance that any one crypt would seed into a well is very near 60% for vertical and horizontal orientations of the crypts as they settle. λ was thus calculated as 0.60*(# of seeded crypts/# of wells).

The number of seeded crypts was assessed in four arrays of 100 wells using light microscopy (Figure 7B). The number of crypts seeding into 125 and 150 μm diameters wells were not assessed as many of the wells were occluded by myofibroblasts and seeding efficiencies were nearly zero (data not shown). Our results demonstrate that circular openings in the base of the microwells nearly doubled the percentage of crypts that seed into the wells compared to solid bottoms for 200 μm diameter wells (7.8±0.5% vs. 3.8±0.5%, $P<0.01$, Figure 7C). Seeding efficiencies in the microstrainers for the 175 μm diameter wells were slightly lower than the 200 μm diameter wells (4.8±1.0% vs. 7.8±0.5%, $P<0.05$, Figure 7C).

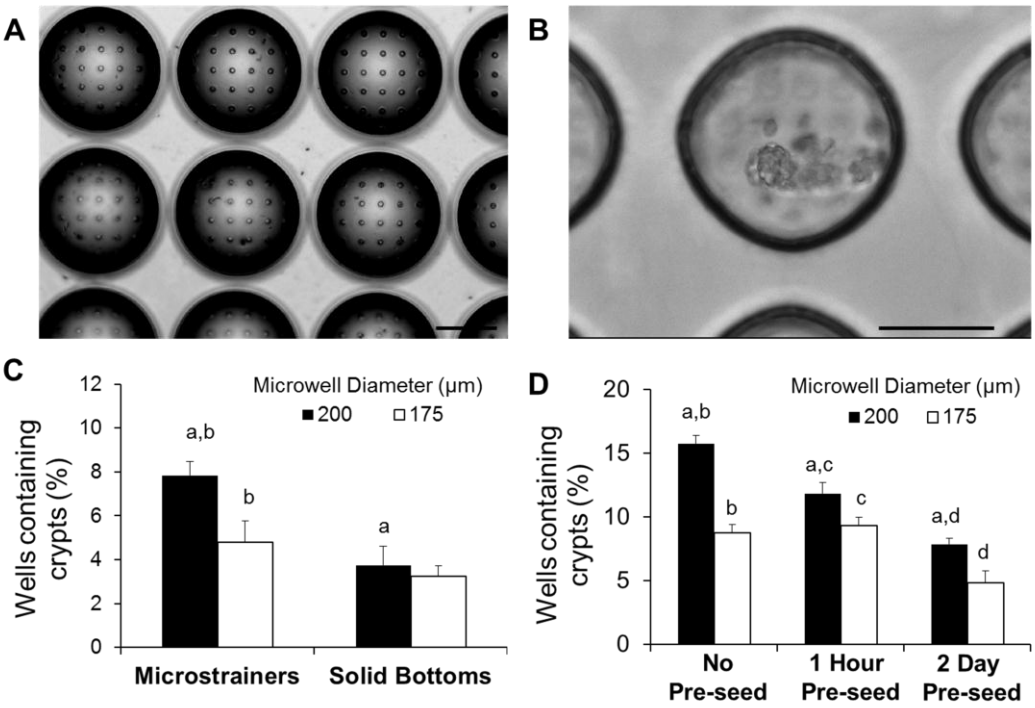

Figure 7. Crypt seeding can be increased with openings in the base of the wells and shortening fibroblast pre-seeding times. Lettering above the bar graphs indicates values that are statistically significant ($p<0.05$) when analyzed with the Student's t-test. Scale bars are 100 μm. A: 200 μm diameter wells with 10 μm circular openings in the well bases. These scaffolds are referred to as "microstrainers." B: Intestinal murine crypts seeded into the microstrainers. C: Seeding efficiency of crypts into microstrainers compared to flat bottom wells for 175 and 200 μm diameter wells. D: Seeding efficiency of crypts into microstrainers for various fibroblast pre-seeding durations. Data are shown as means ± SE (n=4)

Shorter fibroblast seeding times increase crypt seeding efficiency

Although microstrainers increased the number of crypts settling into the wells, seeding efficiency was less than 8%. The efficiency should be approximately 25% based on the geometry of the microwells, the number of seeded crypts, and the Poisson distribution (See Table 2). Light microscopy showed that, as expected, the pre-seeded fibroblasts had attached and spread, obstructing some of the 10 μm openings, which likely limited the flow rate through the wells. We hypothesized that shorter pre-seed durations would result in a higher seeding efficiency. To test this hypothesis, three separate conditions were evaluated. For the first two conditions, myofibroblasts were seeded into the microstrainers at similar densities (30,000 cells/cm$^{2)}$, but the pre-seed durations were varied (i.e., 2 days for the first and 1 hour for the second). In the third condition, myofibroblasts were only seeded along with the crypts, thus, it was the control or "no pre-seed" condition. Intestinal murine crypts were seeded and assessed as described in the previous section. Our results show that seeding efficiencies increase with decreased fibroblast pre-seeding durations. Seeding efficiencies were highest with the "no pre-seed" condition (15.8±0.6%, $p<0.01$), but also increased with the one hour pre-seeding (11.8±0.9%, $p=0.02$) when compared to the two-day pre-seed in the microstrainers (7.8±0.5%, Figure 7D). Seeding efficiencies in the microstrainers were lower in the 175 μm than in the 200 μm diameter well for all pre-seed durations (No pre-seed, 8.8±0.6% vs. 15.8±0.6%, $P<0.01$; 1 hour pre-seed, 9.3±0.6% vs. 11.8±0.9%, $P<0.05$; 2 day pre-seed, 4.8±1.0% vs. 7.8±0.5%, $P<0.05$; Figure 7D)

Key nutrients fully diffuse into the synthetic crypt microwells within 30 minutes

Due to the small geometry of the microwells, there was a need to confirm the *ex vivo* model would be continually supplied with the nutrients glucose and glutamine, which have been shown in previous research to be necessary for intestinal epithelial homeostasis [17]. In the referenced work, rat epithelial cells were found to metabolize 20 nmol glucose/(hr*mg cell dry matter). Factoring in an average cell dry matter mass of 3 ng/cell and the molecular weight of glucose, 180.16 g/mol, the metabolization rate converts to 0.26 ng glucose/(cell*day). The study found the metabolic rate of glutamine to be 17 nmol glucose/(hr*mg cell dry matter) by rat intestinal epithelial cells. With a molecular weight of 146.15, the metabolic rate of glutamine converts to 0.18 ng/(cell*day).

To verify the diffusion, a differential equations fluid modeling software, Comsol, was employed. The convection and diffusion feature in Comsol, which solves the diffusion equation (given below), was selected for this study. A transient analysis was run in Comsol with a duration of four days since media in the cultures is normally changed every 3 to 4 days. The values entered into Comsol are given in Table 3.

$$Diffusion\ equation\colon \frac{\partial \Phi(\mathrm{r},t)}{\partial t} = \nabla \cdot [D(\Phi,\mathrm{r})\nabla\Phi(\mathrm{r},t)]$$

Where: Φ(r,t)=density of the diffusing material at a location ra and time t

$D(\Phi,\mathrm{r})$ is the collective diffusion coefficient for density Φ at location r

∇ represents the vector differential operator del

Table 3. Comsol input parameters.

Comsol input	Value	Basis for chosen value
Diffusion coefficient	$3x10^{-10}$ m^2/s	Diffusion coefficient of glucose in water is $6x10^{-10}$ m^2/s at 25°C. This value was halved for a conservative estimate of glucose and glutamine in DMEM and Matrigel.
Beginning concentration of glucose [and glutamine]	25 mol/m^3 [6 mol/m^3]	4500 mg/L glucose in DMEM. 4mM Glutamine in DMEM supplemented with 2mM GlutaMAX OR No Glutamine in Advanced DMEM/F12 with 6mM GlutaMAX added
Uptake (flux) of glucose [and glutamine] within microwells	$-4.9x10^{-9}$ [$-3.4x10^{-9}$] $mol/(m^2*s)$	Assuming 30,000 cells per sq. cm., the # of cells in each 200 µm well works out to 28. An uptake per cell of 0.26 ng glucose/(cell*day) [calculated above] was also factored in.
Height of media layer	1.27 mm	Based on 10 ml of media in a 10 cm culture dish

Comsol modeling with the given parameters showed that the concentrations of glucose and glutamine should stabilize in the cultures within 30 minutes (data not shown). The diffusion rate varies with the temperature of the fluid, the viscosity of the fluid, and the size of the particle of the diffusing molecule. All else being equal, smaller particles diffuse more rapidly than larger particles. Because glutamine and oxygen are smaller molecules than glucose (molecular weight 146 and 32 vs. 180), their diffusion in DMEM is more rapid than glucose (data not shown).

Supplementing glutamine concentrations may be necessary for proper intestinal epithelial homeostasis

In addition to the diffusion of key nutrients, the total consumption of glutamine and glucose in culture was considered. To determine whether the amount of nutrients provided to the *ex vivo* cultures was sufficient for proper homeostasis, the total amount of each nutrient

supplied and also metabolized was calculated. Oxygen was not a concern as it is in constant supply in the atmosphere provided to the cultures. For glucose and glutamine, the previously calculated values of 0.26 ng glucose/(cell*day) and 0.18 ng glutamine/(cell*day) were used for the consumption calculation. To calculate the total number of cells metabolizing nutrients, both the number of myofibroblasts and the epithelial cells in one sq. cm of the *ex vivo* culture were estimated. Assuming 30,000 myofibroblasts/sq.cm for a flat surface (Figure 5A) and a 350% increase in surface area for wells with 200 μm diameter, 200 μm depth, and 25 μm outside diameter spacing (Table 1), the number of myofibroblasts in one sq. cm is 105,000 for the *ex vivo* cultures. To calculate the number of epithelial cells, the number of crypts and the number cells in each crypt were estimated. The number of 200 μm diameter wells with 25 μm spacing in one sq. cm is 1600. Assuming 250 cells per crypt in a mouse [22], the number of epithelial cells in one sq. cm is 400,000. The rate of nutrient consumption calculated as 131,000 ng glucose/(sq. cm.*day) and 90,000 ng glutamine/(sq. cm.*day).

To calculate the quantity of nutrients supplied to the culture, the concentration of the nutrients and the volume of the media were determined. As stated in Table 3, the concentration of glucose in the media used in this study is 4500 mg/L and glutamine is 6 mM, which converts to 877 mg/L of glutamine. Next, the volume of media supplied to one sq. cm of the *ex vivo* culture was estimated. We assumed 10 mL of media is added to a 10 cm culture plate with a surface area of 78.5 cm^2. The volume supplied to one sq. cm is calculated as 0.127 mL. The amount of glucose and glutamine supplied to one sq. cm of the culture is then calculated as 572,000 ng glutamine and 110,000 ng glutamine. Using the consumption rates/sq.cm calculated above, glucose would be exhausted in 4.4 days and glutamine in 1.2

days. These figures suggest the amount of glutamine supplied to the cultures should be increased to avoid the necessity of changing the media daily.

DISCUSSION

This chapter presents experiments conducted in the development of a 3-D biomimetic scaffold that promotes a monolayer of myofibroblasts and allows the seeding of intestinal crypts into synthetic microwells. The ability of several materials to facilitate adhesion and proliferation was first characterized. Our experiments showed that myofibroblasts cultured on polystyrene, PDLA, and 1002F, proliferated more rapidly than on PDMS. During the culture, the myofibroblasts formed aggregates of cells, leaving portions of the scaffold uncovered for several days on all materials except polystyrene. This cell aggregation was most pronounced on days 2 to 4 after initial cell seeding and likely limited cell proliferation (Figurea 5 A,B,C). Following this initial aggregation and slowed proliferation, the myofibroblasts began dividing to fill intervening opening spaces (Figure 5B). Cell aggregation could be the result of the scaffold becoming more hydrophobic after plasma oxidation as PDMS has been shown to lose charge stability within a few hours [23]. Future studies could explore more advanced ECM coating techniques that promote retention of the scaffold material hydrophilicity. The commercially treated polystyrene was found to promote proliferation more logarithmically linear and more rapid than the other materials. PDMS, PDLA, and 1002F were all treated in the lab with plasma oxidation and ECM coating. To imporove upon the proliferation of myofibroblasts on scaffolds manufactured in a lab setting,

oxidation and ECM coating strategies may need to be standardized and more technologically advanced.

Myofibroblast proliferation was slowest and aggregation most pronounced on PDMS than on all other materials, therefore this material was eliminated as a possible material for the *ex vivo* scaffold. Myofibroblast proliferation was similar on PDLA and 1002F, therefore the proliferation rate does not need to be a consideration when choosing between these two materials.

Experiments were also conducted to determine the dimensions of the microwells that would allow: 1) the formation of a monolayer of fibroblasts; 2) crypts to seed into the microwells; and 3) the diffusion of key nutrients into the microwells. The experiments conducted in this study demonstrated that microwells of 200 μm diameter and depth met the criteria for crypt seeding and nutrient diffusion. Shortening fibroblast seeding times and creating small openings in the bottom of the wells were also shown to enhance seeding efficiencies. Theoretical seeding efficiencies were also calculated based on microwell dimensions, crypt dimensions, the number of seeded crypts, and the Poisson distribution. Comsol analysis showed that glucose and glutamine readily diffuse into the wells. Total nutrient calculations showed that glucose supplied to the cultures is sufficient for four days, but the amount of glutamine should be elevated by increasing either the concentration of glutamine or the volume of the media added to the cultures. These experiments and the seeding efficiency characterization are applicable to lab-on-a-chip, organ-on-a-chip, and tissue engineering applications which involve seeding cells or cell conglomerates into confined spaces.

CHAPTER 3

OPTIMIZATION AND CHARACTERIZATION OF CRYPT ISOLATION

INTRODUCTION

We have recently shown the ability to culture IESCs *in vitro* into enteroids which consist of all four cell lineages of the intestinal epithelium [24]. This culture system is a powerful tool that can be used to study the signaling pathways responsible for proliferation and differentiation of IESCs, study the effects of various pharmaceuticals on epithelial tissue at the cellular level, and expand epithelial tissue for subsequent transplantation into patients whose intestinal epithelium has been damaged by necrotizing enterocolitis, cancer, or other diseases sometimes requiring intestinal tissue resection.

In the creation of this *in vitro* culture, primary epithelial tissue is isolated from murine or other animal models. Many labs, including ours, use a chelation step to isolate the epithelial tissue and this procedure has been studied extensively [25, 26] Despite previous work, the quantity and viability of isolated tissue is highly variable. In addition, the isolation of IESCs has only been accomplished very recently, and the downstream potency of the stem cell population has not been fully characterized [27]. Standardizing the isolation and culture of epithelial tissue and IESCs will facilitate the establishment of quantitative assays to allow more statistically relevant scientific conclusions.

Our strategy was to approach this standardization as a workflow engineering problem and to optimize each step of the process. The isolation step was first examined. The isolation procedure entails incubating the intestinal tissue in EDTA followed by a crucial step in which the tissue is shaken by hand to remove the epithelial layer from the basement membrane. This hand shaking step clearly introduces variability to the isolation procedure. By studying the force and frequency of the shaking procedure, we sought to characterize the amount and viability of tissue isolated, and minimize variability.

If whole crypts are desired, following release from the basement membrane, the tissue is rinsed and is ready for downstream use. Some research studies, however, require single IESCs. To isolate the stem cells, following isolation, the epithelial tissue is dissociated to single cells to allow cell sorting. Typically, dispase has been used for dissociation, however, recent work found that trypsin provided the best balance of dissociation efficiency, viability, and antigen retention for neural cells [28]. In the work presented herein, dispase and trypsin were compared for their ability to dissociate epithelial tissue to single cells while maintaining the integrity of important cell surface receptors CD24 and CD44.

IESCs must be separated from the intestinal tissue by FACSorting to allow single cell culture**.** Tissue from a *Sox9EGFP* reporter gene mouse model was used for the isolation. In previous work, we demonstrated that 'low' levels of Sox9, designated *Sox9EGFP*^{low}, mark cells that are enriched for IESC gene markers including *Lgr5*, *Olfm4*, and *Ascl2* [24]. By design, FACS is meant to preserve the viability of cells, however we had recently learned that hematopoietic cell viability could be increased by changing FACS parameters such as the nozzle size. We sought to determine whether the viability and culture efficiency of IESCs was affected by FACS.

MATERIALS AND METHODS

Mice/Genotyping

All mice used in this study were 6 to 10 weeks old and were maintained on a 12:12-h light-dark cycle in American Association for Accreditation of Laboratory Animal Care-approved facilities. C57BL/6J mice were used for the majority of the experiments and were procured from Jackson Laboratories. Sox9EGFP mice were used for the FACS optimization experiments.

Tissue Isolation

For all experiments, mice were drop anesthetized in isoflurane and sacrificed by cervical dislocation. The small intestine was removed by cutting at the pyloric sphincter and immediately proximal to the cecum. The first 2 cm distal to the pyloric sphincter was designated as the duodenum, which was removed and discarded. The next 10 cm segment (from 2 to 12 cm distal to the pyloric sphincter) was designated the jejunum. This segment was collected and used for all experiments in this study.

Removal from basement membrane

To begin the epithelial isolation and remove mucus, intestinal tissue was first incubated for 20 min on ice in Dulbecco's phosphate buffered saline (DPBS) containing 30 mM ethylenediaminetetraacetic acid (EDTA) and 1.5 mM Dithiothreitol (DTT). The tissue was transferred to a 15 mL conical tube containing 6 mL of DPBS and 30 mM EDTA and incubated at 37^{o}C for 10 min. Tubes were then shaken by hand along their long axis. The

frequency and acceleration of the shakes were measured using the accelerometer in the Apple iPhone. Using Context Logger, a free application available online, the characteristics of the shaking procedure could be viewed in real-time and uploaded into Microsoft Excel. See Figure 8 for examples of the various shaking alternatives tested in this study.

To assess the amount of epithelial tissue removed, the remnant intestinal tissue was Swiss-rolled and fixed in optimal cutting temperature (OCT) compound (Sakura Finetek USA, Inc, Torrance, CA). Tissues were sectioned and stained with Bisbenzimide (Sigma) and an epithelial cell adhesion molecule (EpCAM) antibody preconjugated to Alexa Fluor 647 (Biolegend, San Diego, CA). The entire section was then imaged and analyzed using Image J. The crypts and villi were often removed in continuous sections; therefore, the percent of epithelial tissue removed was measured by summing the length of the sections removed along the longitudinal axis of the intestinal tissue and dividing by the total length of 10 cm.

Separation of crypt cells from villus cells

Due to the relatively small population of crypt cells in the intestinal epithelium, it is sometimes necessary to enrich for either crypt or villus cells. Two different methods of accomplishing this were compared: filtering, and mechanical separation by scraping. In the filtering method, after removing the epithelium from the basement membrane, the epithelial tissue was passed through a 70 μm filter (BD Falcon) with the goal of collecting the villi in the filters and allowing the crypts to pass through. In the scraping method, the intact intestine was first cut into 5 cm segments and everted on to a pasteur pipette. The everted intestine was incubated on ice in a DPBS solution containing 10 mM EDTA and 1 mM DTT

for 5 min then laid flat on a petri dish and each mucosal side was scraped very delicately with a cover slip to remove the villi. Each of the preparations were then dissociated to single cells and analyzed by flow cytometry to determine the corresponding percentages of crypt cells.

Dissociating to single cells

If intestinal epithelial cells are to be analyzed by flow cytometry, dissociating them to single cells is necessary. In the standard protocol, dispase (Collaborative Biomedical, product discontinued) is added to HBSS at 0.3 U/mL and the cell preparation is incubated in this solution for 10 min. Trypsin (TrypLE Express, Invitrogen) was also tested for its ability to dissociate the epithelium to single cells and avoid cleaving important cell surface receptors such as CD24 and CD44. Cell fractions from five WT mice were split in half and dissociated by incubating for 10 min in either dispase or trypsin. Dissociation to single cells was evaluated by counting with the aid of light microscopy and by flow cytometry. For the visual counting, cells from three separate samples were counted under a Zeiss Axiovert 40C microscope. Four separate fields of view were counted for each sample to ensure accurate numbers. Doublets were counted as two cells, and multimers with three or more cells were counted as three and a half. The percent of single cells was then calculated as the number of single cells divided by the total number of counted cells.

For flow cytometry, cells were analyzed under side scatter height versus side scatter area. Single cells fell along a narrow diagonal line in this plot, and the percentage of cells in this population was recorded. Cell fractions were also stained with anti-CD24 preconjugated with Pacific Blue (Biolegend) and anti-CD44 preconjugated with APC/Cy7 (Biolegend)

antibodies and evaluated by flow cytometry for their corresponding percentages of cells expressing the target surface receptors.

FACS

The final step in the systematic evaluation of this protocol was to evaluate the survival rate of epithelial cells after FACS. After dissociating to single cells, cells were filtered through a 40 µm filter and rinsed with HBSS. Cells were then resuspended in Advanced DMEM/F12 (Gibco), with supplements as described in previous work (Gracz, 2009). Cells were stained with propidium iodide (PI, Invitrogen) and sorted by FACS. Dead cells and lymphocytes were excluded by side scatter versus forward scatter, and doublets were excluded by side scatter height versus side scatter area as previously described. Cells positive for PI were then excluded and the PI negative cells were sorted into Advanced DMEM/F12 media with the previously stated supplements and allowed to incubate on ice for 90 min. Cells were stained with PI again and analyzed by flow cytometry.

Statistics

The data are presented as the mean ± SEM.

RESULTS

The removal of epithelial tissue from the intestinal basement membrane can be standardized

One critical and highly variable step in epithelial isolations is the removal of the tissue from the basement membrane of the intestine. After an EDTA soak, the tissue is

typically shaken by hand in a 15 mL conical tube to release the epithelial tissue from the underlying lamina propria. To improve reproducibility between centers, technicians, and experiments, the removal of the epithelial tissue during the hand shaking step was standardized. Three variations of shaking force were tested, classified as low (1 times gravity, 1G), intermediate (2.5G), and high (>2.5G) (Figure 8 A,B,C). The intermediate and high shaking force removed a similar number of cells (29.2±5.0 $x10^6$ vs 35.6±3.9 $x10^6$, p=0.37, Figure 8D). The cells isolated with the intermediate and high shaking force also had similar viabilities (82±1 vs. 87±, p=0.23, Figure 8E), however, a larger percentage of crypts and villi were dissociated to single cells and cell aggregates with the high shaking force. Shaking forces slightly above 2.5g, therefore, are not detrimental to cell viability, and can be employed if intact cell preparations are not desired. Shaking with less force (Figure 8C)

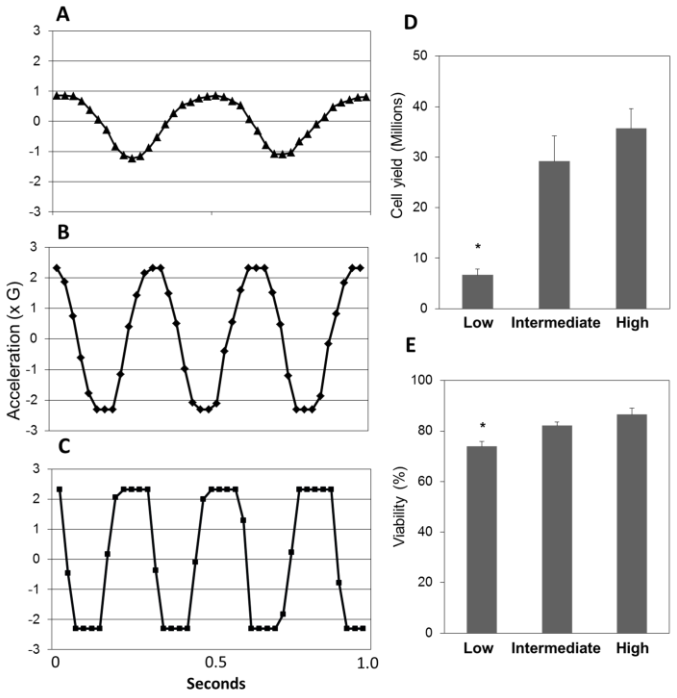

Figure 8. Accelerometer readings, yield, and viability of epithelial cells isolated by various shaking alternatives. Although the accelerometer records acceleration along three axes, the acceleration depicted is along the long axis of the tube and is the key measurement. A: Low shaking force B: Intermediate shaking force C: High shaking force D, E: Yield and viability of cells isolated from 10 cm of jejunum for the 3 shaking alternatives. An asterisk (*) indicates values that are statistically significant when compared to the intermediate force ($P<0.05$). Data are shown as means ± SE (n=3)

produced fewer cells than the intermediate force (6.7±1.1 x10^6 vs. 29.2±5.0 x10^6, $p<0.05$, Figure 8D) and cells were also less viable (73±2 vs 82±1, $p<0.05$, Figure 8E).

The suggested frequency of the shake, between 2.5 and 3 back and forth cycles per second, was chosen to promote a natural rhythmic motion and organically produce the intermediate force. This frequency also allows for 75 to 90 shake cycles in 30 seconds. This number of shake cycles is suggested for its ability to remove a large portion of the crypts, about 80 to 85%.

Mechanical scraping of the intestine facilitates crypt enriched fractions

IESCs constitute less than 1% of total epithelial cell preparations; therefore, sort times can sometimes be several hours. Sort times can be reduced by generating a cell preparation with a larger percentage of crypt cells, i.e. a crypt enriched preparation. To determine whether crypt enrichment is possible and reproducible, two methods were studied and compared to a total epithelial cell preparation: a filtering method, and mechanical separation of the crypts from the villi with a glass cover slip. Since murine intestinal crypts are on average 45 μm in diameter, the hypothesis for the filtering method was that passing the cell solution through a 70 μm filter would filter out the larger villus cell aggregates while allowing the crypts to pass through. During this experiment, light microscopy demonstrated that a large percentage of the epithelial tissue was removed in 'crypt-villus units' consisting of one villi and several attached crypts. Therefore, while filtering out the larger villus pieces, the crypts were also filtered out. To quantify these findings, cell preparations were analyzed by flow cytometry and compared to the standard total epithelial cell preparation. Sox9EGFP intensity was used to identify crypt cells, as nearly all of the GFP cells in this mouse model

are localized to the crypts. Sox9EGFP^{low} and Sox9EGFP^{sublow} fluorescent intensities mark IESCs and transit amplifying cells, respectively, and both cell types are located in the crypts. The analysis paralleled our visual observations and confirmed there was a trend toward de-enrichment of crypts with the filtering method versus the total epithelial preparation (2.18±0.75% vs. 2.45±0.75%)

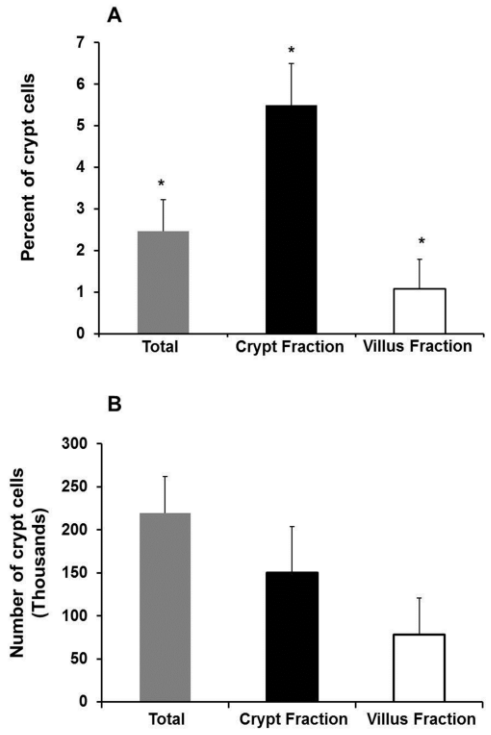

Figure 9. Yield of crypt cells from crypt enriched cell preparations compared with a standard EDTA preparation. Jejunum from Sox9EGFP mice were subjected to the differential scraping method. Crypt cells are defined as those that are Sox9EGFP^{low} and Sox9EGFP^{sublow}. A: The percentage of crypt cells in each of the cell preparations (n=3, P<0.05). Total = total epithelial cell preparation. An asterisk (*) indicates values that are statistically significant (P<0.05) B: The total number of crypt cells collected from 10 cm of jejunum. Data are shown as means ± SE (n=3)

In the scraping method, jejunal tissue was everted and soaked in a 10 mM EDTA solution for 5 min. The tissue was laid flat on a petri dish and very lightly scraped with a glass coverslip to remove the villi. The remnant intestinal segment was then incubated as described earlier and the crypts removed by the hand shaking step.

Light microscope examination of the tissue scraped off with the coverslip demonstrated a portion of the crypts were removed with the villi. Flow cytometry was used as described above to quantify the percentages of crypt cells in each of the cell fractions: the tissue removed during the scraping and the tissue removed during the hand shaking step. Despite the loss of a portion of the crypts, the scraping method produced a 2.25-fold increase

in the percentage of crypt cells compared to the total epithelial preparation (5.50±1.00% vs. 2.45±0.75% P<0.05, Figure 9A). To verify cells were not being lost in the scraping method, the total number of cells isolated by each method was determined. Both the total epithelial method and the scraping method (when totaling the crypt and villus fractions) generated cell preparations with 220,000±50,000 crypt cells (Figure 9B).

Crypt cells remain more viable than villus cells after dissociation

To ensure mechanical scraping of the epithelial tissue was not causing decreased viability of the isolated cells, cell preparations from Sox9EGFP mice were stained with PI and analyzed by flow cytometry. Preliminary experiments showed the scraping procedure generated total cell preparations with viabilities of 64±6%. Previous literature noted the use of an anoikis inhibitor, Y27632 (10 µM, Sigma, #Y0503), during culture to improve viabilities [29]. We hypothesized that viabilities could be improved by adding the

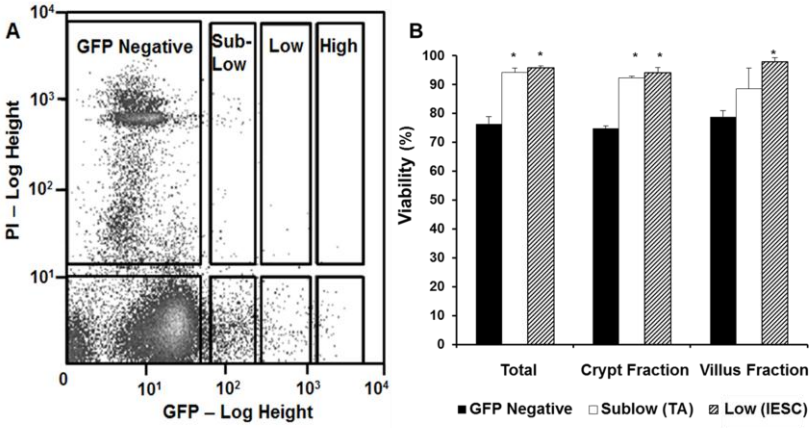

Figure 10. Viability analysis of crypt enriched cell preparations compared with a standard EDTA preparation. A: Flow cytometry plot of a typical total epithelial cell preparation. Rows of boxes depict cell fractions determined by viability (PI positive, upper boxes; PI negative, lower boxes). Columns of boxes show the limits used to identify distinctive cell types based on Sox9EGFP intensity, i.e. Sublow, Low, and High. B: Viabilities of cell populations based on Sox9EGFP intensity. Sox9EGFP^{low} cells are IESCs while Sox9EGFP^{sublow} cells are transit amplifying (TA) cells. An asterisk (*) indicates values that are statistically significan when compared to the GFP Negative cells for each preparation (P <.02). Data are shown as means ± SE (n=3)

anoikis inhibitor to cell solutions immediately after their removal from the mesenchyme. After adding the anoikis inhibitor at this point in the isolation, cell viabilities from the scraping method increased to 86±2%, which is very similar to viabilities from the standard preparation (data not shown).

Interestingly, crypt cells were also observed to be more viable than villus cells. Both the IESCs and the transit amplifying cells, characterized by Sox9EGFP^{low} and Sox9EGFP^{sublow} fluorescent intensity, had cell viabilities of 94±1%, while villus cells, characterized by Sox9EGFP^{neg} fluorescence, had viabilities of 77±1% (Figure 10 A,B).

Trypsin and dispase are equally effective at single-cell dissociation and preserving the integrity of important surface receptors

Dispase has typically been used for dissociation during cell preparations [24]; however, recent work has cited the use of trypsin [30]**.** To determine whether dispase or trypsin produced a higher percentage of single cells, total epithelial cell preparations were split in half and incubated with each reagent. Cells were analyzed for the extent of dissociation to single cells by visual inspection and by flow cytometry. Both analyses produced similar results; that there was a trend for dispase to more fully dissociate preparations to single cells than trypsin (58±4 vs. 51±1 by visual counting; 68±2 vs. 64±2 by flow cytometry; Table 4).

Table 4. Comparison of dissociation by trypsin and dispase.

	Dispase	Trypsin	p value
Single Cells (%)			
-visual counting (n=3)	58 ± 4	51 ± 1	p = 0.25
-flow cytometry (n=5)	68 ± 2	64 ± 2	p = 0.18
$CD24^+$ (%, n=3)	9 ± 1	7 ± 2	p = 0.75
$CD44^+$ (%, n=3)	16 ± 2	16 ± 2	p = 0.81

Proteases have a potential to compromise the integrity of cell surface molecules, which may impact the ability of ligands, peptides, or antibodies to bind to these surface receptors. CD24 and CD44 have been shown to bind differentially to IESCs, [24, 31] therefore preserving these receptors allows IESCs to be distinguished from differentiated cells in the intestinal epithelium in any mouse model. To determine whether trypsin or dispase preserved CD24 and CD44 integrity, cell preparations were stained with anti-CD24 preconjugated with Pac. Blue (Biolegend, Cat# 101820) and anti-CD44 preconjugated with APC (Biolegend, Cat# 103012) and analyzed by flow cytometry. No statistically significant difference was observed between the percent of cells with surface receptors intact when dissociated by dispase or trypsin (9±1 vs 7±2 $CD24^+$, 16±2 vs. 16±2 $CD44^+$, Table 4).

FACS does not reduce IESC viability, as measured by PI

Prior work has shown that when fluorescently sorted IESCs are plated in matrigel with a cocktail of mitogens/morphogens, they form organoids consisting of all four cell types of the intestinal epithelium, which have been termed ‘enteroids’ [24]. These organoids had previously been referred to as cryptoids, however, they are composed of disparate morphologies resembling both crypts and villi. ‘Enteroids’ was therefore chosen as a more accurate descriptor since the prefix entero- denotes relation to the entire intestine.

As stated above, IESC viabilities were greater than 90% at the time of flow cytometric analysis; however, fewer than 5% of the plated IESCs formed enteroids when plated in culture suggesting FACS may be compromising cell viability. To ensure FACS was not reducing viability of IESCs, PI negative, Sox9EGFP^{low} cells were sorted and incubated on ice for 90 min. This duration was chosen as the maximum amount of time between FACSorting and cell plating. The IESCs were post-sort analyzed by the same FACS machine to determine viability based on PI staining. This re-analysis revealed that only 5% of the IESC sorted population had converted to PI-positive status demonstrating FACS conditions did not severely compromise cell viability.

DISCUSSION

In this portion of the work we sought to characterize and optimize the isolation of epithelial cells from mouse models. By making this an engineering workflow problem, the sources of variability in the protocol were isolated. In the initial isolation step, which involves a hand shaking procedure, various forces of shaking were shown to cause differential yields and viability of epithelial tissue. These differences could be sources of error for any research study that includes tissue obtained by different technicians or in multiple research centers. The method of tissue isolation from the basement membrane, therefore, must be carefully defined when creating protocols for research studies.

In this study, the ability to differentially isolate crypt cells and villus cells was demonstrated using a mechanical scraping step. This procedure is useful for any study that seeks to compare differences between crypt and villus cells, or enrich for either population.

Future work could focus on optimizing the durations and EDTA concentrations during the chelation step and could lead to increased enrichment of crypt and villus cells.

Dissociation methods were also compared. Dispase and trypsin were found to be relatively similar in their ability to dissociate to single cells and maintain cell surface receptors, although there was a trend for a more complete dissociation to single cells by dispase. Further studies could expand the list to include other surface receptors important for intestinal epithelial research including CD166, CD29, and CD133; and also compare the dissociation efficacy of trypsin and dispase on human tissue. These studies are useful to translational medicine applications where dissociation of collected epithelial issue is required for downstream transplantation or analysis.

Finally, the effect of FACSorting on stem cell viability was tested. Using Propidium iodide as an indicator, we demonstrated that FACSorting does not significantly affect the viability of IESCs. Further studies with other apoptosis and annoikis markers such as Annexin V may be required to better understand the effect of FACS on the ability of IESCs to be successfully cultured *in vitro* or *ex vivo*.

CHAPTER 4

IMAGING STRATEGIES

INTRODUCTION

Standard light microscopy is only capable of capturing two-dimensional surfaces. Three-dimensional imaging is required to facilitate recapitulation of the 3-D environment and allow analysis of live tissue in the *ex vivo* model. Multi-photon excitation (MPE) imaging was utilized as it is capable of penetration depths that allow the imaging of the 200 μm deep synthetic crypt microwells used in this study. The MPE microscope employs a series of lenses to focus light photons from a laser on a precise location of the sample. Light is only emitted from this location and is then captured by the microscope. The laser is refocused to scan the entire horizontal 2-D plane within the tissue. Successive 2-D planes are scanned until the desired 3-D tissue is imaged.

MPE imaging offers several features which are beneficial for the *ex vivo* model. MPE is more compatible with imaging live tissue cultures because it results in less photodamage than laser scanning or spinning disk confocal microscopy [32]. In addition, MPE imaging is capable of precise signal discrimination, which produces more accurate images of the color emissions from a sample. Recent MPE work has shown the ability to distinguish each of the intestinal cell lineages using autofluorescence alone and without immunohistochemistry staining [33].

To create accurate 3-dimensional renderings of the *ex vivo* models, images captured with MPE need to be processed with sophisticated image analysis software. Imaris was utilized because it is a powerful 3-D and 4-D analysis tool that uses filtering, space filling, and identification algorithms to render and track cells spatially and temporally. These capabilities facilitate the development of representative renderings and quantitative analysis of the imaged tissue. This chapter details the use of MPE and Imaris to image and render the myofibroblasts on the 3-D scaffolds.

MATERIALS AND METHODS

Sample Preparation

Myofibroblasts (P10 from 4 to 6-day-old CD-1 pups, isolated as described in Chapter 1) were plated on PDLA scaffolds with microwells with 200 μm diameter and depth. After fixing with 4% PFA, cells were stained with the following: Bisbenzimide (Sigma); and the antibodies primary anti-Vimentin (Aves Labs, Tigard, Oregon), and secondary Alexa-549 (Jackson ImmunoResearch, West Grove, PA).

System Specifications

An Olympus Fluoview 1000 MPE microscope with a MaiTai DeepSee laser with less than 100 femtosecond pulses was utilized to image the *ex vivo* cultures. The microscope was fitted with a 25x, 1.05 numeric aperture, water immersion objective with a 2 mm working distance. The MPE uses a non-descanned detection system and has four photomultiplier detectors [BFP (420-460nm), GFP (495-540nm)GFP, RFP (575-630nm) RFP, and wide

range BFP,CFP, GFP, YFP (380-560)]. These features provide efficient signal detection with very minimal loss.

RESULTS

Multi-photon imaging paired with Imaris rendering produced accurate 3-dimensional models of ex-vivo cultures

Preliminary images with 2-D light microscope images of the *ex vivo* models (Figure 11A,B) did not allow analysis of the cellular morphology within the microwells, therefore MPE imaging was employed. To determine the settings necessary for accurate MPE imaging, samples were prepared as described in the Materials and Methods section, and laser emission wavelengths were modified to determine wavelengths that would produce the brightest images. The secondary fluorophore stain that was used, AlexaFluor 549, was found to have the brightest emissions when excited with laser emission wavelengths of 920

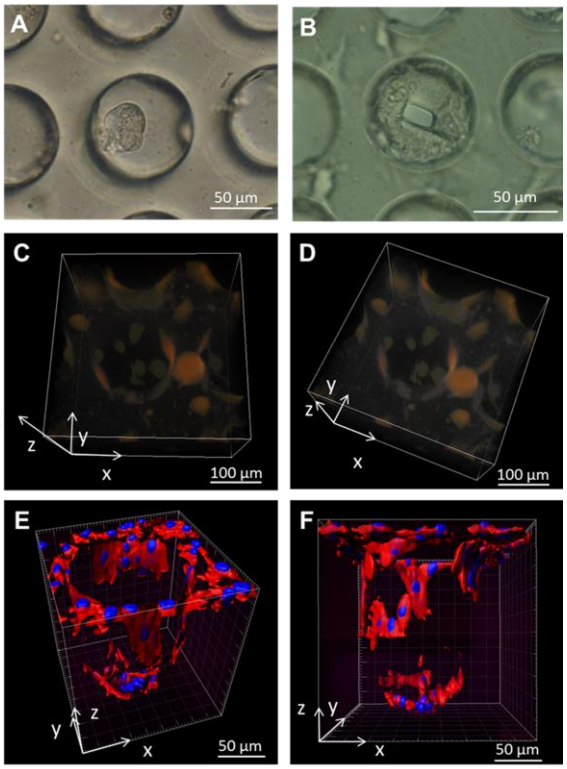

Figure 11. Imaging within the microwells. X,Y, and Z indicate the orientation of each image. A,B: Brightfield image of myofibroblasts and epithelial cells cultured in microwells. C,D: Myofibroblasts in an array of microwells imaged with a MPE microscope. Cytoplasm is depicted in orange. E,F: Myofibroblasts in a single microwell imaged with a MPE microscope and rendered with Imaris. Cell nuclei are blue and cytoplasm is red.

nanometers.

With MPE imaging, the entire extent of the imaged cell membranes were not captured (Figure 11 C,D). To improve upon this detail and visualize more of the extent of the plated cells, the rendering software Imaris was employed. With more advanced space filling and filtering capabilities, Imaris was able to produce images that depicted a greater extent of the cellular cytoplasm in the *ex vivo* cultures (Figure 11 E,F). In the generation of the space-filled models, Imaris requires the input of several parameters, most notably the 'surface detail' and 'smallest sphere which fits into object.' The optimal values of each of these parameters can vary depending on the size and orientation of the cells within the microwells, however, values near 2.0 μm for the 'surface detail' and 2.5 μm for the 'smallest sphere which fits into object' produced images that were most representative of the rendered tissue cultures in this research.

Multi-photon imaging confirms some microwells are occluded by myofibroblasts

Initial observations from light microscopic examination of the ex vivo models suggested that myofibroblasts occluded many of the microwell openings. To verify this occlusion, myofibroblasts were seeded onto the scaffolds at 60,000 cells/sq. cm and cultured for two days as described earlier. MPE imaging paired with Imaris renderings confirmed initial observations that the microwells had varying areas of occlusion by the myofibroblasts. Figure 12 depicts completely open wells (A,B), partially open wells (C,D), and closed wells (E,F).

DISCUSSION

In this portion of the research, we sought to develop strategies for recapitulating the 3-D morphology of live tissue in *ex vivo* models. Using MPE imaging, paired with Imaris rendering software, accurate renderings of myofibroblasts on the scaffolds were produced. We also confirmed initial observations that various amounts of myofibroblasts occluded the microwell openings. The Imaris settings cited for modeling in this work can be used for tissue engineering, organ-on-a-chip, or any other research necessitating renderings of cells on a 3-D surface.

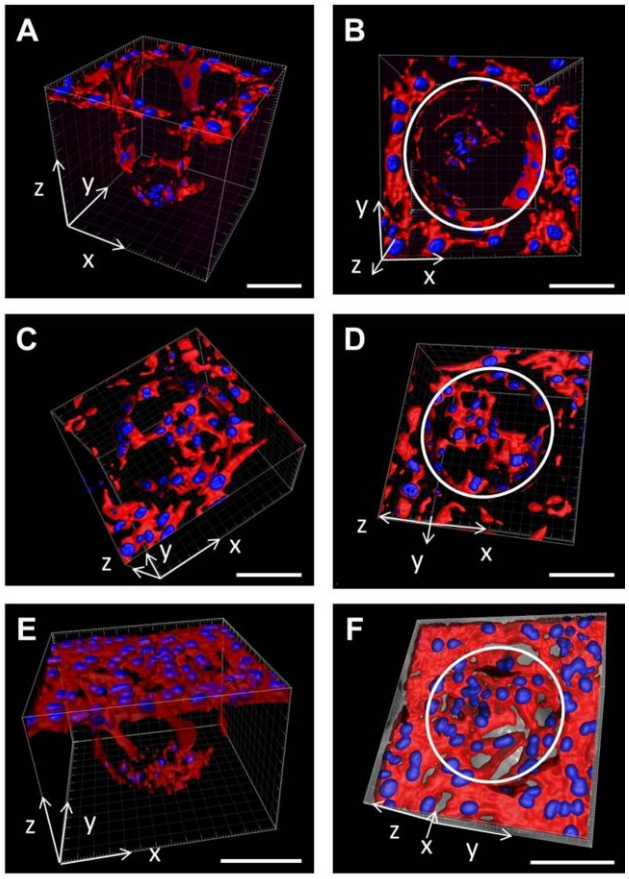

Figure 12. Imaris renderings confirm varying open areas of the microwells. X,Y, and Z indicate the orientation of each image. All scale bars are 100 µm. Cell nuclei are blue and cytoplasm is red. Limits of the well opening are shown with a white ring. A,B: Completely open well. C,D: Partially occluded well; open area is greater than the cross-sectional area of a vertical crypt. E,F: Fully occluded well.

While the imaging results presented in this work are qualitative, MPE and Imaris techniques could be used to gather quantitative results of *ex vivo* model experiments. When combined, these imaging and rendering tools allow the study of cellular migration, protein filament formation, and high resolution fluorophore intensity discrimination. These capabilities can be used to examine extra cellular matrix formation, the interactions between epithelial and mesenchymal layers, and stem cell commitment to progenitor and functional cell lineages. In addition, 'super-

resolution' microscopy techniques, such as 4Pi and ANSOM, could be employed and are capable of imaging molecules 4 to 10 times smaller than those capable with MPE [34]. This increased resolution could allow the study of vesicle trafficking or the transport of cell surface receptor targeted pharmaceuticals across the plasma membrane and into cell endosomes, lysosomes, or nuclei.

CHAPTER 5

CONCLUSIONS AND FUTURE WORK

This body of work details preliminary research in the development of an *ex vivo* model of the crypts of the small intestine. Important scaffold parameters were evaluated including the material choice, synthetic crypt microwell dimensions, and nutrient supply. We were also successful at establishing isolation, seeding, and imaging techniques that can be used as a stepping stone for eventual development of the model. Further work could include more exhaustive testing of the proliferation and biocompatibility of the gut myofibroblasts and epithelial cells with various biomaterials, varying the geometric design of the scaffold, and more precise methods of positioning crypts within the microwells.

The work presented herein showed the biocompatibility of gut myofibroblasts with PS, PDLA, and 1002F. Further work could focus on testing a more broad set of materials for the scaffold. Previous research has shown the ability to test cellular attachment, proliferation rates, and proper gene expression on microarrays capable of testing hundreds of materials at a time [35]. Similar tests with gut myofibroblasts and epithelial cells on the microarrays could reveal materials that provide more advantageous surface properties and gene expression patterns than the materials tested herein.

The geometry of the scaffold used in this study was a very simple rectangular array of circular microwells. This surface geometry left large intervening spaces between the wells. Minimizing these intervening spaces would likely increase seeding efficiencies of the crypts into the microwells and could facilitate the development of an epithelial layer that more

closely mimics the endogenous environment. To minimize the intervening spaces, the microwells could be a hexagon shape and/or arranged in a more staggered geometry. Hexagon shapes are very structurally sound and space saving geometry as evidenced by their natural occurrence in organic compounds and honeycomb. The hexagon shape may also allow for easier integration of areas for villi in the *ex vivo* model.

Even with improvements to the geometry and the high spatial detail capable with microfabrication, recreating the complex extra cellular matrix microanatomy of the crypts and villi of the small intestine will be a complex and onerous process. Decellularized organ components may need to be incorporated into the scaffold design as they have been shown to provide the architecture and proteins that promote proper cellular proliferation and differentiation [36] and many of the tissue engineering successes to date have used this type of supporting structure [37, 38]. Recent research has also shown that the crypt/villus architecture of the small intestine can be maintained by decellularizing with detergent-enzymatic treatment [39]. Decellularized organs have the added benefit of providing a mix of ECM proteins that are advantageous to proper cellular proliferation.

Regardless of the scaffold design, the precise and systematic placement of correctly oriented crypts in the scaffold will be advantageous to develop a functional epithelial layer. Because of the crypts flared shape at their open end, they are not subject to symmetric fluid dynamics; therefore, a carefully calibrated flow of liquid through the microwells could accurately orient the crypts. Another option that has been gaining traction in the tissue engineering field is the use of 3-D printing technologies which utilize retrofitted inkjet or similar printing devices to print scaffold materials or live tissue [40, 41]. Bio-ink printing technologies have also been developed to allow the assemblage and precise placement of

cells in desired shapes and locations [42, 43]. Dielectrophoresis could also be explored as it has been shown to successfully position live cells in high-density arrays [44].

REFERENCES

1. Baker, M., *Tissue models: a living system on a chip.* Nature, 2011. 471(7340): p. 661-5.

2. Ghaemmaghami, A.M., et al., *Biomimetic tissues on a chip for drug discovery.* Drug Discov Today, 2012. 17(3-4): p. 173-81.

3. Huh, D., et al., *Reconstituting organ-level lung functions on a chip.* Science, 2010. 328(5986): p. 1662-8.

4. Mahler, G.J., et al., *Characterization of a gastrointestinal tract microscale cell culture analog used to predict drug toxicity.* Biotechnol Bioeng, 2009. 104(1): p. 193-205.

5. Imura, Y., K. Sato, and E. Yoshimura, *Micro total bioassay system for ingested substances: assessment of intestinal absorption, hepatic metabolism, and bioactivity.* Anal Chem, 2010. 82(24): p. 9983-8.

6. Kedinger, M., et al., *Cellular and molecular partners involved in gut morphogenesis and differentiation.* Philos Trans R Soc Lond B Biol Sci, 1998. 353(1370): p. 847-56.

7. Kedinger, M., et al., *Importance of a fibroblastic support for in vitro differentiation of intestinal endodermal cells and for their response to glucocorticoids.* Cell Differ, 1987. 20(2-3): p. 171-82.

8. Khademhosseini, A., et al., *Co-culture of human embryonic stem cells with murine embryonic fibroblasts on microwell-patterned substrates.* Biomaterials, 2006. 27(36): p. 5968-77.

9. Gupta, K., et al., *Lab-on-a-chip devices as an emerging platform for stem cell biology.* Lab Chip, 2010. 10(16): p. 2019-31.

10. Kim, K.A., et al., *Mitogenic influence of human R-spondin1 on the intestinal epithelium.* Science, 2005. 309(5738): p. 1256-9.

11. Sung, J.H. and M.L. Shuler, *Microtechnology for Mimicking In Vivo Tissue Environment.* Ann Biomed Eng, 2012.

12. Zhou, J., A.V. Ellis, and N.H. Voelcker, *Recent developments in PDMS surface modification for microfluidic devices.* Electrophoresis, 2010. 31(1): p. 2-16.

13. Pai, J.H., et al., *Photoresist with low fluorescence for bioanalytical applications.* Anal Chem, 2007. 79(22): p. 8774-80.

14. Berthier, E., E.W. Young, and D. Beebe, *Engineers are from PDMS-land, Biologists are from Polystyrenia.* Lab Chip, 2012.

15. Wang, Y., et al., *Benchtop micromolding of polystyrene by soft lithography.* Lab Chip, 2011. 11(18): p. 3089-97.

16. Grikscheit, T.C., et al., *Tissue-engineered small intestine improves recovery after massive small bowel resection.* Ann Surg, 2004. 240(5): p. 748-54.

17. Beaulieu, A.D., et al., *Isolated canine and murine intestinal cells exhibit a different pattern of fuel utilization for oxidative metabolism.* J Anim Sci, 2002. 80(5): p. 1223-32.

18. Wang, Y., et al., *Microdevice to capture colon crypts for in vitro studies.* Lab Chip, 2010. 10(12): p. 1596-603.

19. Gong, S., et al., *A gene expression atlas of the central nervous system based on bacterial artificial chromosomes.* Nature, 2003. 425(6961): p. 917-25.

20. Widera, D., et al., *Adult palatum as a novel source of neural crest-related stem cells.* Stem Cells, 2009. 27(8): p. 1899-910.

21. Puliafito, A., et al., *Collective and single cell behavior in epithelial contact inhibition.* Proc Natl Acad Sci U S A, 2012. 109(3): p. 739-44.

22. Kellett, M., C.S. Potten, and D.A. Rew, *A comparison of in vivo cell proliferation measurements in the intestine of mouse and man.* Epithelial Cell Biol, 1992. 1(4): p. 147-55.

23. Kim, B., K.P. ET, and I. Papautsky, *Long-term stability of plasma oxidized PDMS surfaces.* Conf Proc IEEE Eng Med Biol Soc, 2004. 7: p. 5013-6.

24. Gracz, A.D., S. Ramalingam, and S.T. Magness, *Sox9 expression marks a subset of CD24-expressing small intestine epithelial stem cells that form organoids in vitro.* Am J Physiol Gastrointest Liver Physiol, 2010. 298(5): p. G590-600.

25. Bjerknes, M. and H. Cheng, *Intestinal epithelial stem cells and progenitors.* Methods Enzymol, 2006. 419: p. 337-83.

26. Bjerknes, M. and H. Cheng, *Methods for the isolation of intact epithelium from the mouse intestine.* Anat Rec, 1981. 199(4): p. 565-74.

27. Formeister, E.J., et al., *Distinct SOX9 levels differentially mark stem/progenitor populations and enteroendocrine cells of the small intestine epithelium.* Am J Physiol Gastrointest Liver Physiol, 2009. 296(5): p. G1108-18.

28. Panchision, D.M., et al., *Optimized flow cytometric analysis of central nervous system tissue reveals novel functional relationships among cells expressing CD133, CD15, and CD24.* Stem Cells, 2007. 25(6): p. 1560-70.

29. Sato, T., et al., *Single Lgr5 stem cells build crypt-villus structures in vitro without a mesenchymal niche.* Nature, 2009. 459(7244): p. 262-5.

30. Sato, T., et al., *Paneth cells constitute the niche for Lgr5 stem cells in intestinal crypts.* Nature, 2011. 469(7330): p. 415-8.

31. Hou, N.Y., et al., *CD133+ CD44+ subgroups may be human small intestinal stem cells.* Mol Biol Rep, 2011. 38(2): p. 997-1004.

32. So, P.T., et al., *Two-photon excitation fluorescence microscopy.* Annu Rev Biomed Eng, 2000. 2: p. 399-429.

33. Orzekowsky-Schroeder, R., et al., *In vivo spectral imaging of different cell types in the small intestine by two-photon excited autofluorescence.* J Biomed Opt, 2011. 16(11): p. 116025.

34. Huve, J., et al., *4Pi microscopy of the nuclear pore complex.* Biophys J, 2008. 95(2): p. 877-85.

35. Anderson, D.G., S. Levenberg, and R. Langer, *Nanoliter-scale synthesis of arrayed biomaterials and application to human embryonic stem cells.* Nat Biotechnol, 2004. 22(7): p. 863-6.

36. Barakat, O., et al., *Use of decellularized porcine liver for engineering humanized liver organ.* J Surg Res, 2012. 173(1): p. e11-25.

37. Song, J.J. and H.C. Ott, *Organ engineering based on decellularized matrix scaffolds.* Trends Mol Med, 2011. 17(8): p. 424-32.

38. Wu, S., et al., *Human urine-derived stem cells seeded in a modified 3D porous small intestinal submucosa scaffold for urethral tissue engineering.* Biomaterials, 2011. 32(5): p. 1317-26.

39. Totonelli, G., et al., *A rat decellularized small bowel scaffold that preserves villus-crypt architecture for intestinal regeneration.* Biomaterials, 2012.

40. Baran, E.T., et al., *Microchannel-patterned and heparin micro-contact-printed biodegradable composite membranes for tissue-engineering applications.* J Tissue Eng Regen Med, 2011. 5(6): p. e108-14.

41. Gaetani, R., et al., *Cardiac tissue engineering using tissue printing technology and human cardiac progenitor cells.* Biomaterials, 2012. 33(6): p. 1782-90.

42. Jakab, K., et al., *Tissue engineering by self-assembly of cells printed into topologically defined structures.* Tissue Eng Part A, 2008. 14(3): p. 413-21.

43. Jakab, K., et al., *Tissue engineering by self-assembly and bio-printing of living cells.* Biofabrication, 2010. 2(2): p. 022001.

44. Hsiung, L.C., et al., *A planar interdigitated ring electrode array via dielectrophoresis for uniform patterning of cells.* Biosens Bioelectron, 2008. 24(4): p. 875-81.